Article

Cell Chemical Biology

Iron Biochemistry is Correlated with Amyloid Plaque Morphology in an Established Mouse Model of Alzheimer's Disease

Graphical Abstract

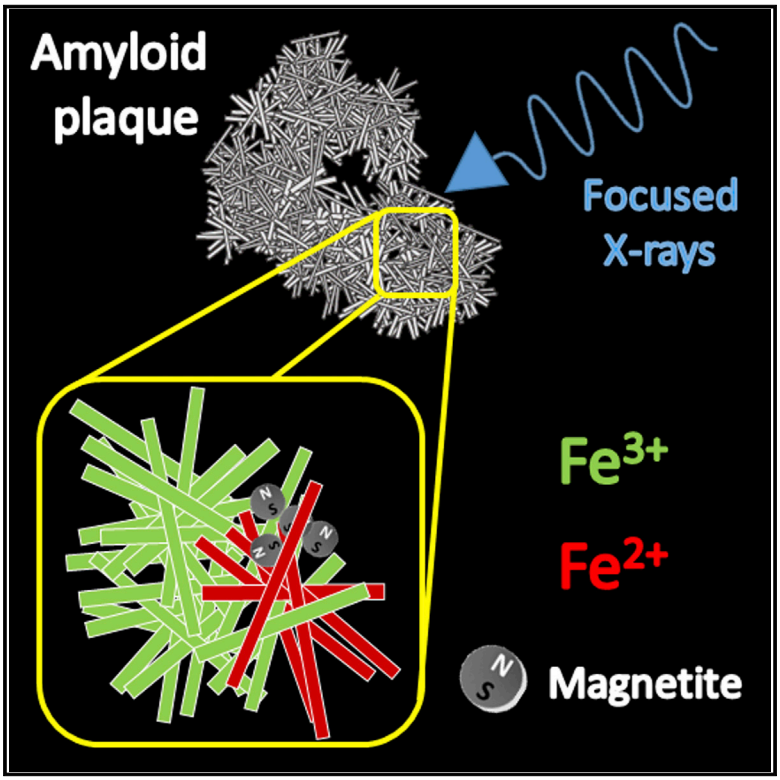

Authors

Neil D. Telling, James Everett, Joanna F. Collingwood, ..., Joseph J. Gallagher, Jian Wang, Adam P. Hitchcock

Correspondence

n.d.telling@keele.ac.uk

In Brief

Telling et al. demonstrate an enhanced role for iron in Alzheimer's disease pathology, having implications for neurodegeneration, early-stage diagnosis by MRI, and possible treatments based on metal chelation.

Highlights

- Chemically reduced pure ferrous iron is directly associated with amyloid pathology
- Diffuse amyloid deposits could comprise an iron-amyloid complex
- Magnetic signature of particulate magnetite detected with varying oxidation state

Telling et al., 2017, Cell Chemical Biology *24*, 1205–1215
October 19, 2017
http://dx.doi.org/10.1016/j.chembiol.2017.07.014

CellPress

Cell Chemical Biology
Article

Iron Biochemistry is Correlated with Amyloid Plaque Morphology in an Established Mouse Model of Alzheimer's Disease

Neil D. Telling,[1,9,*] James Everett,[1] Joanna F. Collingwood,[2,3] Jon Dobson,[3,4] Gerrit van der Laan,[5] Joseph J. Gallagher,[6] Jian Wang,[7] and Adam P. Hitchcock[8]
[1]Institute for Science and Technology in Medicine, Keele University, Stoke-on-Trent, Staffordshire ST4 7QB, UK
[2]Warwick Engineering in Biomedicine, School of Engineering, University of Warwick, Coventry CV4 7AL, UK
[3]Department of Materials Science and Engineering, University of Florida, Gainesville, FL 32611, USA
[4]J. Crayton Pruitt Family Department of Biomedical Engineering, Institute for Cell Engineering and Regenerative Medicine (ICERM), University of Florida, Gainesville, FL 32611, USA
[5]Magnetic Spectroscopy Group, Diamond Light Source, Didcot, Oxfordshire OX11 ODE, UK
[6]Department of Physiology, Trinity College Institute of Neuroscience, Trinity College Dublin, Dublin, Ireland
[7]Canadian Light Source Inc., 44 Innovation Boulevard, Saskatoon, SK S7N 2V3, Canada
[8]BIMR and Department of Chemistry, McMaster University, Hamilton, ON L8S 4M1, Canada
[9]Lead Contact
*Correspondence: n.d.telling@keele.ac.uk
http://dx.doi.org/10.1016/j.chembiol.2017.07.014

SUMMARY

A signature characteristic of Alzheimer's disease (AD) is aggregation of amyloid-beta (Aβ) fibrils in the brain. Nevertheless, the links between Aβ and AD pathology remain incompletely understood. It has been proposed that neurotoxicity arising from aggregation of the $Aβ_{1-42}$ peptide can in part be explained by metal ion binding interactions. Using advanced X-ray microscopy techniques at submicron resolution, we investigated relationships between iron biochemistry and AD pathology in intact cortex from an established mouse model over-producing Aβ. We found a direct correlation of amyloid plaque morphology with iron, and evidence for the formation of an iron-amyloid complex. We also show that iron biomineral deposits in the cortical tissue contain the mineral magnetite, and provide evidence that Aβ-induced chemical reduction of iron could occur *in vivo*. Our observations point to the specific role of iron in amyloid deposition and AD pathology, and may impact development of iron-modifying therapeutics for AD.

INTRODUCTION

The accumulation of the peptide fragment amyloid-beta ($Aβ_{1-42}$) within the brain is a characteristic hallmark of Alzheimer's disease (AD) (Selkoe, 1994; Yanker and Lu, 2009). It appears that the neurotoxicity of Aβ is linked to its aggregation state and subsequent involvement in redox cycles (Rival et al., 2009). Further, studies have suggested that the interaction of metal ions such as iron and aluminum with Aβ, and also copper and zinc, could play a crucial role in the release of reactive oxygen species (ROS) that contribute to neurodegenerative damage (House et al., 2004; Khan et al., 2006; Smith et al., 1997). In particular, iron can exist in both redox-active forms (as ferrous, Fe^{2+} iron) and redox-inactive forms (as ferric, Fe^{3+} iron). The aggregation state of $Aβ_{1-42}$ appears to affect the binding of Fe^{2+} and Fe^{3+} and thus influences the iron redox cycle and consequently the release of free radicals via Fenton chemistry (House et al., 2004; Khan et al., 2006; Rival et al., 2009). *In vitro* studies have also demonstrated that this coexistence of iron and Aβ decreases cell viability, confirming this enhanced toxicity (Liu et al., 2011; Rottkamp et al., 2001; Wan et al., 2011).

Evidence for a link between the accumulation of redox-active iron in the AD brain and the oxidative damage caused by ROS, has profound implications for understanding the progression and treatment of the disease. To date, redox-active iron minerals such as magnetite (Fe_3O_4) have been found within tissue extracted from human Alzheimer's brain (Collingwood et al., 2005, 2008; Kirschvink et al., 1992), and in brain tissue sections from APP/PS1 transgenic mice (Gallagher et al., 2012). In addition, our recent *in vitro* studies have built on prior work confirming the formation of redox-active ferrous iron and nanocrystalline magnetite following the aggregation of Aβ with ferric iron in different forms (Everett et al., 2014a, 2014b). However direct evidence for the *in vivo* role played by Aβ in the iron redox cycle and the formation of redox-active minerals, remains elusive.

The presence of localized iron *in vivo* can be detected by MRI due to its effect on the surrounding tissue, giving rise to detectable changes in transverse relaxation (T2) and susceptibility. It is therefore possible that the presence of iron in AD tissue could be used as a diagnostic tool (Acosta-Cabronero et al., 2013; Antharam et al., 2012; Dobson, 2001; El Tannir El Tayara et al., 2007; Meadowcroft et al., 2009, 2014; Wang et al., 2014). Crystalline magnetic minerals such as magnetite can strongly affect MRI contrast. The relative impact of mineralized iron deposits on MRI parameters depends very much on the materials

properties of the deposits (including crystallinity, iron oxide phase, and size distribution), and the extent to which the deposits are aggregated or disbursed within tissue (Collingwood and Telling, 2016). It is therefore important to determine which forms of iron are associated with different pathology in AD, in order to interpret MRI data for the assessment of disease progression. Further to this, emerging drug treatments based on iron chelation, such as deferiprone (Devos et al., 2014), are dependent for their efficacy on how strongly the iron is bound *in vivo*, i.e., whether molecular or crystal bonding exists, together with the morphology and surface structure of the iron deposits.

In this study we investigated the oxidation state and distribution of nanoscale iron *in situ* in cortical tissue, taken from an APP/PS1 transgenic mouse model that reproduces the amyloid deposition characteristic of AD. To probe both iron oxidation and magnetic state we exploited techniques that use the element-specific X-ray absorption of soft X-rays (Regan et al., 2001; van der Laan, 2013; van der Laan and Figueroa, 2014), defined as having energies between 40 and 2000 eV. Scanning transmission X-ray microscopy (STXM), which combines spectroscopic analysis with high-resolution microscopy, has been used in applications as diverse as catalysis (de Groot et al., 2010), microbiology (Coker et al., 2012; Hunter et al., 2008), and biomaterials (Leung et al., 2010). In particular, previous studies have used STXM to map the oxidation state of iron in different environments (Coker et al., 2012; Hunter et al., 2008; Tone et al., 2009) an approach that is also used here.

In addition to the oxidation state, element-specific magnetism can be detected by measuring the difference in absorption when using X-rays of either left or right circular polarization (van der Laan, 2013; van der Laan and Figueroa, 2014). This difference is known as X-ray magnetic circular dichroism (XMCD) and occurs at specific absorption edges such as the iron $L_{2,3}$ edges. The characteristic XMCD spectrum of magnetite (Telling et al., 2009; van der Laan, 2013; van der Laan and Figueroa, 2014) enables its unambiguous identification, even when crystallographic information is not available, or when the mineral is combined or co-located with other non-magnetic iron oxides. Further, XMCD obtained using STXM provides a powerful combined microscopic probe that can measure oxidation and magnetic state, and identify different mineral phases on the nanometer scale (Coker et al., 2012; Hunter et al., 2008). We present the use of X-ray spectromicroscopy in combination with TEM, to determine the oxidation state, magnetic state, and morphology of iron deposits and their relation to pathological features in AD tissue.

RESULTS AND DISCUSSION

Mapping Protein Structure in Embedded Sections with X-Ray Spectromicroscopy

Semi-thin adjacent sections of transgenic mouse tissue, taken from a region encompassing the entorhinal cortex (see Supplemental Information; Figure S7) were examined using STXM, with the X-ray energy tuned to specific absorption features. Protein (i.e., tissue) maps using the C K-edge π^* amide peak (288.2 eV) were obtained of the area surrounding iron deposits prior to measuring high-magnification iron maps, as shown in Figure 1A. However, in order to obtain sufficiently thin (<500 nm) specimen sections for STXM measurements it was necessary to embed the tissue in a resin. Most TEM resins contain carbon groups that produce peaks exactly overlapping the tissue (protein) peaks, thus destroying contrast in the protein maps.

To avoid this problem we utilized a specialist resin developed for use in STXM imaging that has been characterized elsewhere (Li et al., 2009). The effectiveness of this resin is demonstrated in Figure S1 (Supplemental Information). Characteristic carbon K-edge X-ray absorption spectra were obtained in a region of the sample containing mainly tissue, and a region containing mainly resin (Figure S1A). It can be seen from the figure that the spectrum from the tissue area contains a significant contribution from the resin (as expected for embedded tissue) and does not closely resemble a reference protein C K absorption edge spectrum (Figure S1C). However by scaling the resin spectrum to the pre-edge shoulder in the tissue peak and then subtracting the spectra, it is possible to recover a protein spectrum very similar to the reference sample (Figures S1B and S1C). In particular, the post edge peak (labeled * in Figure S1) can be clearly seen even though this is not easily discernible in the raw spectrum from the tissue.

For a given sample it was therefore possible to obtain protein maps of the tissue by subtracting images obtained at the X-ray energy corresponding to a strong resin feature (red arrow in Figure S1A), from those obtained at the π^* amide protein peak (blue arrow in Figure S1A). The resin-subtracted images thus obtained expose the protein structure (i.e., tissue) in the sections, as shown for a cortical section of the wild-type mouse tissue sample in Figures S1D–S1I. As can be seen from this figure, the obtained protein maps reveal detail of the cellular membranes, organelles, and extracellular matrix, while surface artifacts (such as the glue contamination seen in Figures S1D and S1E) are removed.

Analysis of Morphology and Oxidation State of Iron

Following a coarse (low spatial resolution) survey of several adjacent sections from both wild-type and transgenic samples, we examined in detail 15–20 areas of 50 × 50 μm^2 for each sample type where the sections appeared intact, and where these areas were spaced evenly over a total tissue section area of several mm^2. Areas containing iron deposits were identified by obtaining iron maps over regions where dense deposits could be discerned, as demonstrated for a section from the wild-type sample in Figures S2A–S2C. Using this procedure it was possible to detect iron deposits down to ~100 nm in size within areas measuring ~25 × 25 μm^2.

In total, evidence for only four iron oxide deposits was found in the areas examined in the wild-type tissue sample. One of these (not shown) was several micrometers in size with straight edges and was of sufficient thickness to fully absorb X-rays at the Fe L_3 absorption edge. This deposit was thus considered to be particulate surface contamination and was not analyzed further in this study. The other three iron deposits, shown in Figures S2D–S2F, appear symmetrical in nature and are approximately 100–300 nm in size. In contrast, we found numerous dense deposits in the tissue sections from the transgenic mouse sample. However due to time constraints it was only possible to probe a representative proportion of these with the X-ray techniques. The absence of substantial iron deposits in the wild-type tissue suggests that the use of 0.1 M sodium cacodylate in the tissue

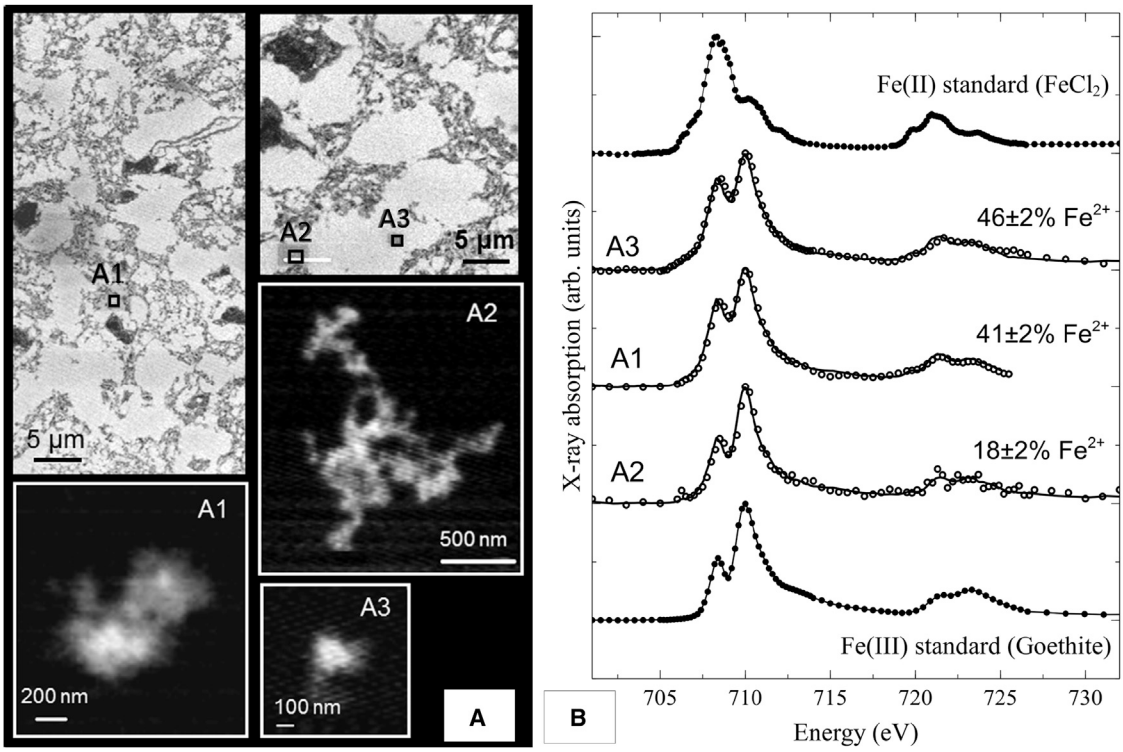

Figure 1. Spectromicroscopy Analysis of Spatial Distribution, Morphology, and Oxidation State of Iron Deposits within Protein Structure

(A) Protein maps (top) obtained from a cortical section of transgenic mouse tissue showing three areas (A1, A2, and A3) where iron deposits were located. Corresponding high-magnification iron maps of these deposits are also shown (lower images).

(B) X-ray absorption intensity measured across the Fe $L_{2,3}$ absorption edge obtained from the iron deposits shown in (A). Also shown in (B) are the absorption spectra obtained from an Fe^{3+} reference standard (in this case the iron oxyhydroxide, goethite FeO(OH)), and an Fe^{2+} reference standard ($FeCl_2$). The strongest peak intensity was normalized to unity for each spectrum for ease of comparison. The solid line for the spectra from regions A1–A3 corresponds to a best fit using a superposition of suitably scaled Fe^{2+} and Fe^{3+} X-ray absorption spectra (see Figure S3). See also Figures S1 and S2.

preparation did not lead to iron accumulation in these samples, despite prior work which has indicated that sodium cacodylate (dimethylarsinic acid) can mobilize iron from horse spleen ferritin *in vitro* (Ahmad et al., 2000).

All of the deposits from the wild-type tissue displayed Fe $L_{2,3}$ X-ray absorption spectra identical to that shown in Figure S2G. Comparison with the reference Fe(III) mineral (goethite) in Figure S2G indicates that the iron deposits in the wild-type sample contain predominantly ferric (Fe^{3+}) iron. This is confirmed both by the correspondence of the peak positions, and the reproduction of the characteristic shoulder on the low energy side of the main L_3 peak (which is also reflected at the L_2 absorption edge). Although the exact intensity of this shoulder feature is found to vary for different iron (III) minerals, it is typically approximately half the height of the main L_3 peak.

More extensive tissue damage was seen in the transgenic mouse sample than in the wild-type sample (Figures 1A and S1); however, it is not clear if this damage is pathological or due to tissue fragility during sample preparation. In any case, high-magnification iron maps of iron deposits in regions, labeled A1, A2, and A3 in Figure 1A, revealed a clear fine structure to these deposits. The oxidation state of these iron deposits was investigated using X-ray absorption spectra obtained from spectromicroscopy measurements (Figure 1B).

The oxidation state of iron affects the intensity of the various X-ray absorption peaks measured at the iron L_3 and L_2 absorption edges, as the electron transitions involved are sensitive to the local electronic structure (van der Laan and Kirkman, 1992). This leads to distinct differences in the shape of the X-ray absorption spectrum obtained from Fe^{2+} and Fe^{3+} ions (as seen in the case of the reference spectra labeled curves A and B, respectively, in Figure S3, panel 1). In particular, considering only the L_3 absorption region where the effects can be seen more clearly, Fe^{2+} ions show a strong peak at ~708 eV and a broader shoulder at ~710 eV, while Fe^{3+} ions show a strong peak at ~710 eV with a weaker should at ~708 eV (indicated by dashed vertical lines in Figure S3). It is thus possible to distinguish these two oxidation states of iron using the $L_{2,3}$ absorption spectrum. Further, it is also possible to determine the presence of Fe^{2+} ions within a region containing Fe^{3+} ions, simply by considering the superposition of the spectra. An illustration of this is shown in Figure S3 (panel 1) where the reference curves have been added together in different proportions.

To obtain a more quantitative measure of the percentage of Fe^{2+} ions within an iron deposit, i.e., the ratio $Fe^{2+}/(Fe^{2+} + Fe^{3+})$, it was necessary to allow for the different X-ray absorption cross-sections of the two ion types. This was done by scaling the measured X-ray absorption spectra for Fe^{2+} and Fe^{3+} ions, as

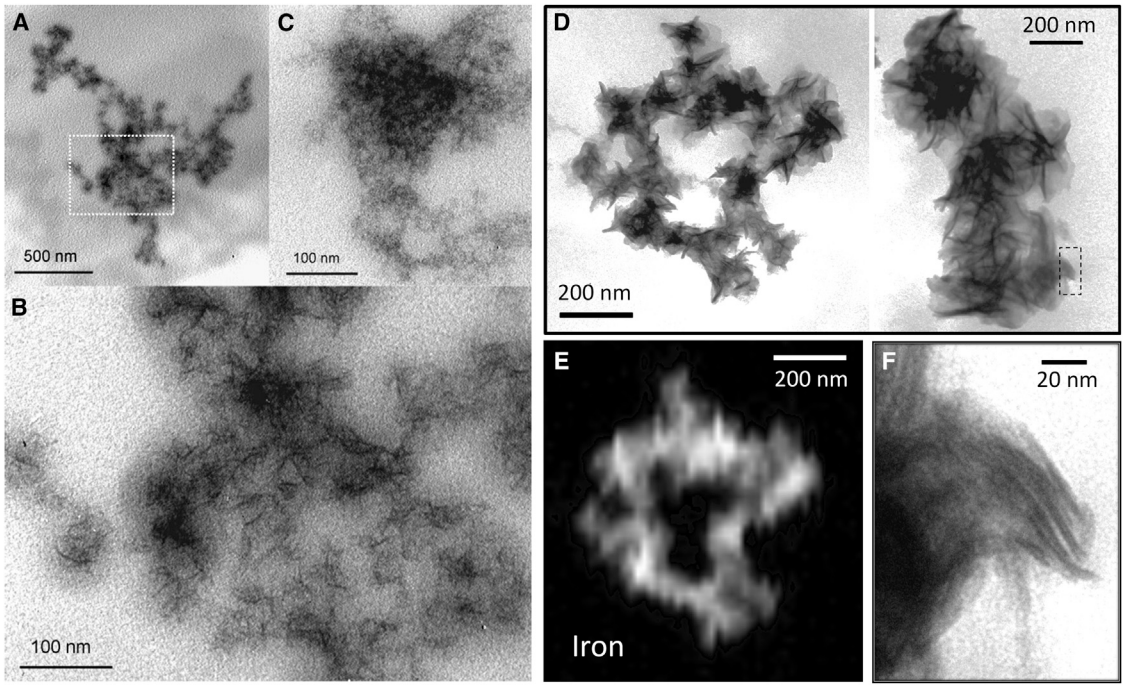

Figure 2. Comparison of TEM and STXM Micrographs Showing Correlation of Iron with Amyloid-like Fibril Morphology

(A–C) TEM images from the unstained section measured by STXM in Figure 1, showing fine structure in regions A2 (A) and (B), and A3 (C). The high-magnification image shown in (B) was obtained from the dotted area shown in (A).

(D–F) Part (D) shows unstained TEM images of fibrillar structures located in a nearby area of the same section. The iron-containing fragment shown in (D) was observed initially by TEM and subsequently mapped using STXM; iron map shown in (E). A higher-magnification TEM image of the dashed box region in (D) is shown in (F). See also Figure S3.

shown in Figure S3 (panel 2). To determine the percentage of Fe^{2+} ions from each X-ray absorption spectrum measured from the mouse tissue, we performed a non-linear least-squares fitting procedure using the weighting of the spectra shown in Figure S3 (panel 2) as fit parameters. From the fits shown in Figure 1B it can be seen that, while one area (A2) contained predominantly ferric iron, the other areas showed evidence of a substantial ferrous iron component (nearly 50% Fe^{2+} for region A3).

Following STXM examination, high-magnification TEM images were obtained from areas A2 and A3 (Figure 1A), as shown in Figure 2. The TEM images in Figures 2A–2C reveal a structure with a fine fibrous morphology within the iron deposits. In particular, the ferrous iron-containing area (A3) shows very fine structure with an almost amorphous morphology. TEM images from a nearby area in the same section, not originally examined by STXM, revealed numerous dense fragments with a fibrillar morphology typical of amyloid plaques obtained from AD tissue (Meadowcroft et al., 2009), and containing fibrils of between 50 and 150 nm in length (Figures 2D–2F). A subsequent STXM examination of one of these fragments confirmed a direct correspondence between the iron density (in this case determined by STXM to be ferric iron) and fibril density from TEM (see Figures 2D and 2E). Image cross-correlation analysis performed on the images shown in Figures 2D and 2E confirmed a strong correlation of pixel intensity between the images with a coefficient, R = 0.91 (20 nm pixel size), suggesting the fibrils themselves contained iron as opposed to the presence of discrete iron foci within fibril aggregates. A high-magnification micrograph of a thinner area (Figure 2F) revealed fibrils of ~5 nm width that appear typical of cross-beta-amyloid conformation (Fandrich et al., 2011).

Correlation of Iron with Protein Structure

In an adjacent section to that discussed above, some large dense fragments reminiscent of amyloid plaque deposits were observed. Combined protein and iron maps covering the area around these deposits are shown in Figures 3A and 3B. Careful examination of the protein map in Figure 3A reveals that the iron-bearing dense fragments shown in Figure 3B also appear in the protein map and must thus contain substantial concentrations of protein or peptide. However, when C K-edge X-ray absorption spectra were obtained for these regions (Figure 3C), a broadening of the π^* amide peak was evident, compared with the spectrum measured from the surrounding tissue (which is also identical to the amyloid peptide spectrum [Everett et al., 2014b]). The presence of iron should not affect the protein X-ray absorption spectrum directly, as the energy is well below the Fe $L_{2,3}$ absorption edge and so X-ray absorption from the iron should be minimal. We hypothesize that the observed peak broadening in the protein spectrum may arise from modification of the amyloid structure due to the formation of an iron-amyloid composite.

We were able to exploit this peak broadening to obtain maps at an alternative energy (labeled P2 in Figure 3C) just below the π^* amide peak (labeled P1). The resulting map using the P2

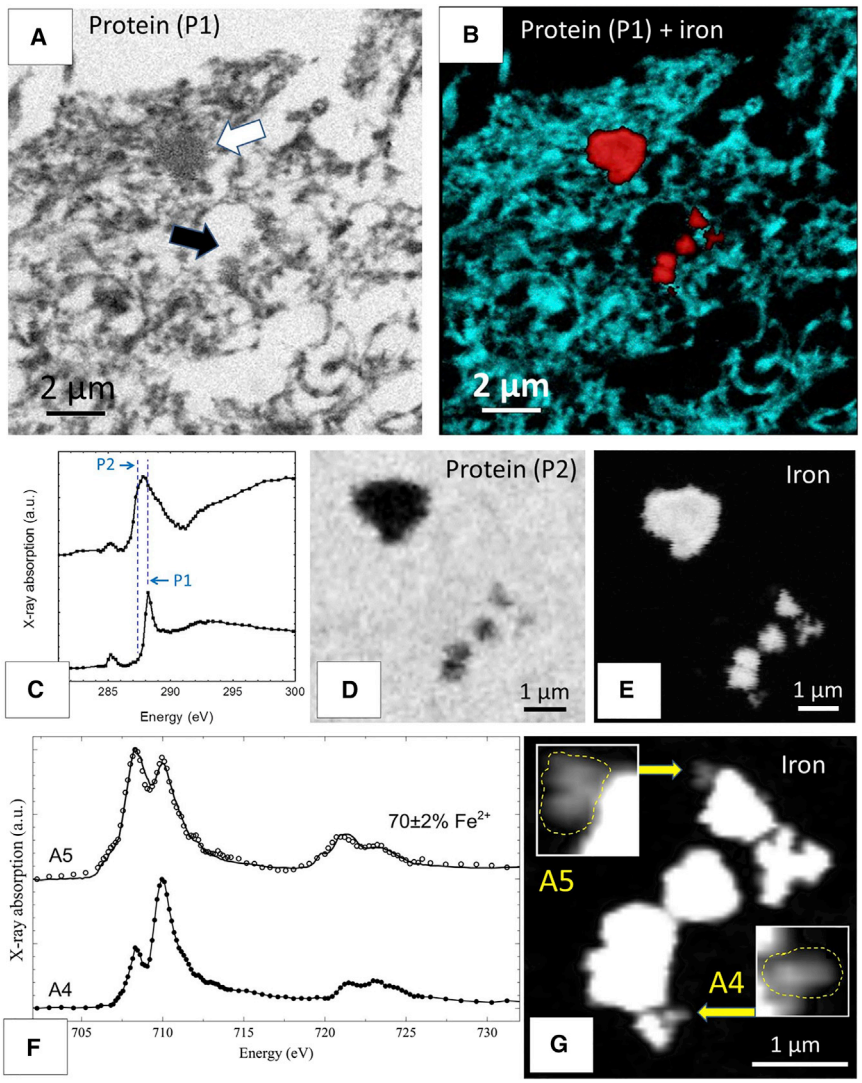

Figure 3. Spectromicroscopy Analysis of Co-located Protein and Iron

(A and B) Protein map obtained from unstained cortical section of transgenic mouse tissue (arrows show the location of iron-bearing fragments) (A); false color composite protein (cyan) and iron (red) map (B) from the region shown in (A).

(C) Carbon K-edge X-ray absorption spectra from the iron-loaded region (top) and surrounding tissue (bottom).

(D) Protein map obtained using the alternative X-ray energy position, P2, shown in (C).

(E) Iron map from the same region as in (D); also used in the composite image in (B).

(F and G) Iron $L_{2,3}$ X-ray absorption spectra (F) obtained from thin areas A4 and A5 shown as enlarged insets with positions indicated by the yellow arrows in (G). The solid line for the spectrum of region A5 corresponds to a best fit using a superposition of suitably scaled Fe^{2+} and Fe^{3+} X-ray absorption spectra (see Figure S3). See also Figure S4.

feature in the broadened protein spectrum is shown in Figure 3D. Comparison with the iron map in Figure 3E reveals that the material displaying the P2 protein spectral feature is exclusively associated with the iron-rich areas. Although most of this material was too dense for spectral analysis of the iron, it was possible to obtain Fe $L_{2,3}$ X-ray absorption spectra from two thin regions in the smaller fragments (Figures 3F and 3G). One of these regions (A5) clearly contained a substantial ferrous (Fe^{2+}) iron component determined from the fit to constitute ~70% of the iron present (Figure 3F). Further examples of such regions where iron was found to be co-located with protein structure are shown in Figure S4. In all these additional regions, a similar broadening of the π^* amide peak was observed wherever iron was co-located with protein.

In a nearby region on the same section we found a structure resembling a diffuse amyloid plaque (Dickson and Vickers, 2001) (Figure 4). Using the same methodology outlined above it was possible to independently map the three following signals throughout this region: tissue (using the usual P1 spectral peak); material exhibiting the broadened protein spectrum (using the P2 spectral feature); and iron-containing material (Figures 4A and 4B). Both the diffuse plaque and the plaque fragments shown in Figure 3 are consistent in size and morphology with plaques imaged previously using immunofluorescent techniques from age-matched APP/PS1 transgenic mice in the same series as the animal used in the current study (Gallagher et al., 2012).

From the images in Figures 4A and 4B, it appears that the iron distribution exactly matches the plaque morphology. A detailed mapping of the bottom right portion of the plaque-like structure using the weaker Fe L_2 absorption edge to avoid saturation, revealed a near-exact correlation between the intensity (i.e., density) of the signal mapped using the P2 protein spectral feature (Figure 4D), and that of the iron (Figure 4E), with an image cross-correlation coefficient of R = 0.97 (125 nm pixel size). This is consistent with the interpretation that the diffuse plaque is also comprised of a combined material containing both amyloid and iron, as suggested earlier for the fibrillar fragments observed by TEM.

In Situ Combined Nanoscale Measurements of Iron Oxidation and Magnetism

On adjacent semi-thin sections taken from the same transgenic sample we found particulate iron deposits that showed a strong spatial variation in iron oxidation state over regions as small as ~50 nm, an example of which is shown in Figure 5. Iron $L_{2,3}$ X-ray absorption spectra taken from representative regions in the deposit are shown in Figure 5F. For these weaker intensity spectra, which were obtained with a coarse energy step size, it was necessary to first convolve the spectra from Figure S3 (panel 2) with a Gaussian function (σ = 0.2) prior to fitting. From the fits shown in Figures 5F and 5A, substantial variation in the

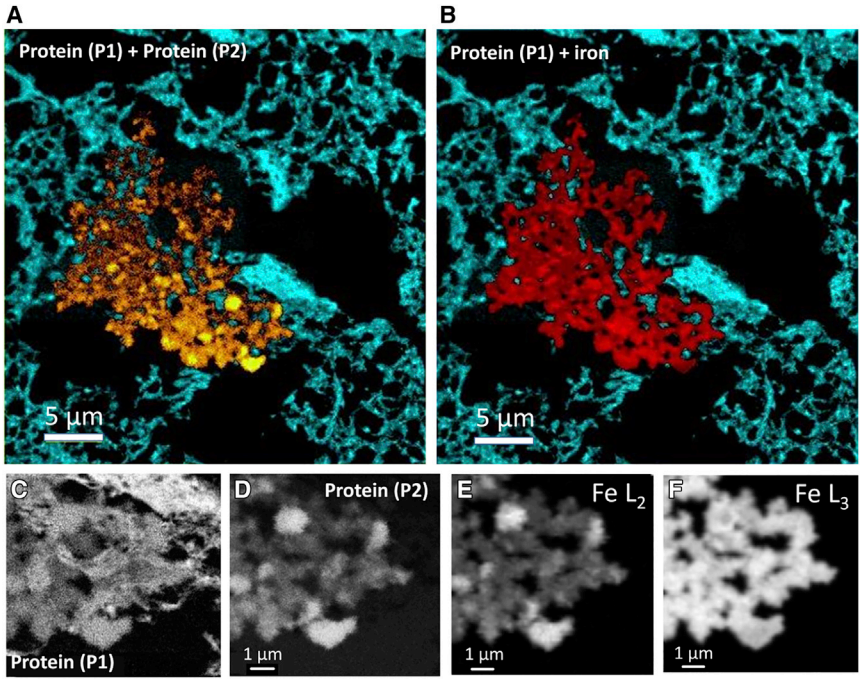

Figure 4. Spectral Imaging Showing Correlation of Protein with Iron in a Feature Resembling a Diffuse Amyloid Plaque

(A) False color composite protein map from an unstained cortical section of the transgenic mouse tissue. The cyan-colored map was obtained using the spectral peak labeled P1 in Figure 3C, whereas the gold-colored map was obtained using the spectral feature labeled P2 in Figure 3C.

(B) False color composite protein (P1, cyan) and iron (red) map obtained from the same region as (A), using the iron L_3 absorption peak.

(C–F) Lower images show enlarged high-resolution protein maps measured using the spectral features P1 and P2, (C) and (D); and iron maps using peaks at the iron L_2 and L_3 absorption edges (E) and (F), respectively. The iron map in (F) is saturated and does not therefore reveal the true iron density variation that can be seen in (E).

Fe oxidation state was determined, ranging from predominantly ferric iron (region B1), to nearly pure (92%) ferrous iron (region B4).

It would seem unlikely that such variations are caused by the coincidental surface contamination of the deposit area by numerous small (~50–200 nm) particles of different oxidation state iron minerals (Dobson and Grassi, 1996). We also discount a postmortem oxidation effect caused by variations in the iron deposit thickness, as the measured optical density values, which are directly proportional to the deposit thickness, indicated that regions B1 and B4 were of approximately the same thickness. In additional experiments on ferric iron standards we further ruled out iron reduction caused by either (1) the preparation of semi-thin sections of material for STXM and TEM analysis, or (2) the interaction of the X-ray beam with the sample during STXM measurements. To do this we prepared embedded sections of iron (III) minerals using identical procedures to those used for the tissue samples. We also deposited samples of these Fe(III) mineral types directly onto electron microscope grids, in order to assess the potential of the X-ray beam to reduce Fe(III) surface contaminants.

The X-ray absorption spectra obtained during STXM measurements for both of these embedded and surface-exposed samples are given in Figure S5, and are entirely consistent with expectations from previously published data (Regan et al., 2001). The X-ray beam dwell time (exposure time) used for these measurements was increased to three times that used for the tissue iron deposits, making beam damage (iron reduction) even more likely in these control experiments. Despite this, no obvious reduction from a pure Fe^{3+} valence state was found for either mineral (Figure S5). Further, the spectra obtained from the embedded samples were almost identical to those seen for the surface deposits, ruling out sample preparation as a possible cause for the iron reduction.

The implicit assumption in the previous fitting analysis is that the Fe^{2+} and Fe^{3+} ions originate from different phases within the iron region being measured; for example, as would occur when a ferric iron deposit had been partially reduced. However, the presence of mixed valence crystalline materials, such as the magnetic mineral magnetite, complicates this simple picture. To detect the presence of such materials, XMCD was used as this is sensitive only to magnetic minerals. By remounting the above section onto a cylindrical permanent magnet and exploiting the circular polarization of the X-ray beam, we were thus able to measure the magnetic properties of this iron deposit, *in situ*.

The circular polarization-dependent X-ray absorption spectra measured under the applied magnetic field are shown in Figure 6A. The corresponding XMCD spectra obtained by subtracting the spectra for the two polarizations, are shown in Figure 6B. The X-ray absorption and XMCD spectra obtained from a synthetic magnetite standard sample (labeled M in Figure 6) are typical for this mineral, with the XMCD spectrum displaying a characteristic negative-positive-negative peak structure due to the ordering of magnetic cations (Coker et al., 2012; Telling et al., 2009; van der Laan, 2013; van der Laan and Figueroa, 2014). The appearance of these features thus indicates the presence of crystalline and ordered magnetite, while the relative intensity of the different peaks in the XMCD spectrum reveals the degree of oxidation (i.e., the ratio of Fe^{2+}:Fe^{3+} cations) of the mineral.

By examining the spectra from the different regions in the tissue it was possible to elucidate dramatic variations in their oxidation and magnetic states. The fraction of Fe^{2+} cations in the magnetic mineral regions was quantified by fitting calculated XMCD spectra to the data in Figure 6B (Telling et al., 2009). Assuming that the magnetite reference sample was stoichiometric with a corresponding Fe^{2+}/Fe^{3+} cation ratio of 0.5, it was found that the three other regions that showed a magnetic (XMCD) response yielded approximate Fe^{2+}/Fe^{3+} ratios of 0.7 (B6), 0.4 (B4), and 0.1 (B5). Here, ratios >0.5 indicate reduction, while those <0.5 indicate oxidation from stoichiometric magnetite.

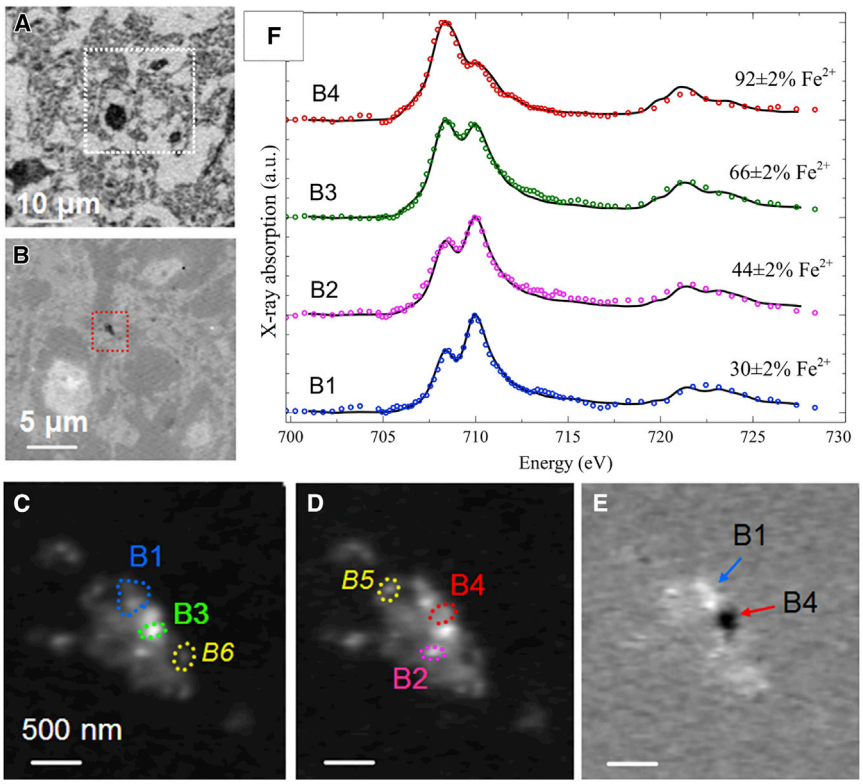

Figure 5. Spectromicroscopy Identification of Local Oxidation State Variations in Nanoscale Particulate Iron

(A) Protein map showing the area surrounding an iron oxide deposit in a cortical section from the transgenic mouse sample.

(B–F) Higher-magnification image (B) of the boxed region in (A), taken at an energy of 350 eV and showing the iron deposit (dotted red box). Iron maps recorded using (C) the prominent Fe^{2+} peak (708 eV) and (D) the prominent Fe^{3+} peak (710 eV) were used for the difference map in (E), which was obtained by subtracting image (C) from image (D), and shows localized regions of Fe^{3+} (bright contrast) and Fe^{2+} (dark contrast). The corresponding Fe $L_{2,3}$ X-ray absorption spectra obtained from the regions labeled B1–B4 are shown in (F). The solid lines for the spectra B1–B4 correspond to best fit curves using a superposition of suitably scaled Fe^{2+} and Fe^{3+} X-ray absorption spectra (see Figure S3). See also Figure S5.

Taking into account all the spectra in Figures 5F and 6, together with the above Fe^{2+}/Fe^{3+} ratios, it was possible to build a profile of the oxidation state of both magnetic and non-magnetic iron phases present in each region of the iron deposit shown in Figures 5B–5E. From this it appears that, whereas one region (B1) contained only a non-magnetic Fe^{3+} phase consistent with ferrihydrite, regions B4 and B6 both contained a reduced form of magnetite together with a non-magnetic Fe^{2+} iron phase, while region B5 contained a heavily oxidized form of magnetite (i.e., approaching the maghemite, Fe_2O_3, stoichiometry). This colocation of different nanoscale iron oxides provides evidence for a possible redox cycling of the iron.

Several similar particulate iron oxide deposits were found in adjacent sections that were examined by TEM. In all cases these deposits were located in electron-dense regions of several microns in size that were generally non-fibrillar (amorphous) in nature. A typical example is shown in Figure 7 where an iron oxidation state map was obtained for the deposit region (Figure 7C) and compared with the TEM image (Figure 7B). From these images it can be seen that the most electron-dense area in the TEM image (Figure 7B) corresponds to an Fe^{2+}-rich region with an X-ray absorption spectrum (not shown) very similar to region B4 in Figure 5. Thus, it is possible that the Fe^{2+} region in Figure 7 also contains nanoscale magnetite, although we do not have comparable XMCD measurements to confirm this. Further examples of regions with a similar morphology and containing particulate nanoscale iron deposits are presented in Figure S6.

In summary, using a combination of X-ray and electron microscopy we have observed the first direct evidence for iron-bearing fibrillar aggregates, together with the iron loading of diffuse plaques at the nanoscale level *ex vivo*. These results, in addition to the modification of the peptide spectrum obtained from the plaques, suggest the composition of diffuse plaques to be that of an iron-amyloid complex. This interpretation supports previous *in vitro* studies that suggest a link between $A\beta_{1\text{-}42}$ aggregation and iron accumulation (Everett et al., 2014a, 2014b; Liu et al., 2011). In particular the short, disordered fibrils tending to an amorphous structure, observed here, are remarkably similar to Aβ fibrils obtained *in vitro* where amyloid was allowed to aggregate in the presence of iron (Everett et al., 2014b; Liu et al., 2011). These and other *in vitro* studies suggest that iron could be fundamentally involved in amyloidosis (House et al., 2004; Huang et al., 2004; Mantyh et al., 1993).

While there are well-documented differences between amyloid deposition in the transgenic APP/PS1 mouse model of AD, and the amyloid deposition observed in human cases of AD, the observations to date *in vitro* and *in vivo* support the hypothesis that there is a fundamental process whereby available iron is chemically reduced in the presence of aggregating Aβ under physiological conditions. The observations presented here, obtained using advanced synchrotron X-ray microscopy techniques, provide the strongest evidence to date that the iron chemistry observed *in vitro* is replicated *in vivo* in a transgenic model of Alzheimer's disease that is directly relevant to the hypothesis being tested, and these findings are consistent with observations in material extracted from human brains exhibiting Alzheimer's pathology (Collingwood et al., 2008; Plascencia-Villa et al., 2016).

However, *in vivo*, it is still not clear whether iron seeds plaque formation or is integrated at a later stage. In the results presented here we observed different types of iron-bearing structures; dense amorphous regions containing localized particulate iron deposits (including magnetite-based minerals), fibrillar fragments, and diffuse plaque morphology. In the latter two cases we found a direct nanoscale correlation between protein/fibril

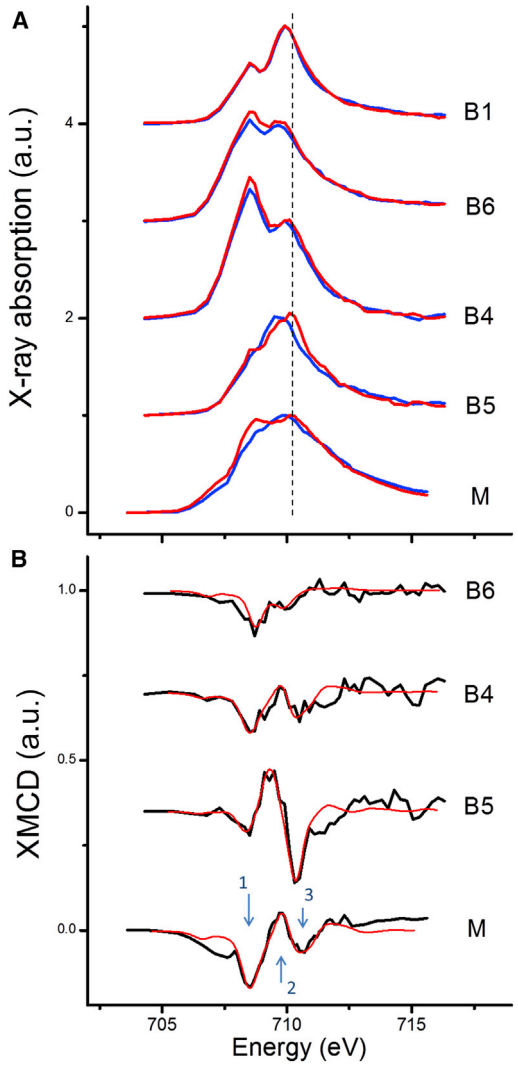

Figure 6. *In Situ* Magnetic Characterization of Particulate Iron Using STXM-XMCD

(A) Fe $L_{2,3}$ X-ray absorption spectra obtained using X-rays with left circular polarization (LCP, blue curves) and right circular polarization (RCP, red curves) for the different regions labeled in Figure 5, together with a reference standard of magnetite nanoparticles embedded in resin (labeled M).

(B) Corresponding XMCD spectra obtained by subtracting RCP curves from LCP curves. The positive and negative peaks labeled 1–3 in the magnetite reference spectrum in (B) are related to: magnetic Fe^{2+} cations on octahedral symmetry sites (1); magnetic Fe^{3+} cations on tetrahedral symmetry sites (2); and magnetic Fe^{3+} cations on octahedral symmetry sites (3). The solid red curves in (B) show an approximate fit of the calculated XMCD spectrum for each region. All spectra were recorded in a magnetic field of approximately 50 mT applied parallel to the X-ray beam.

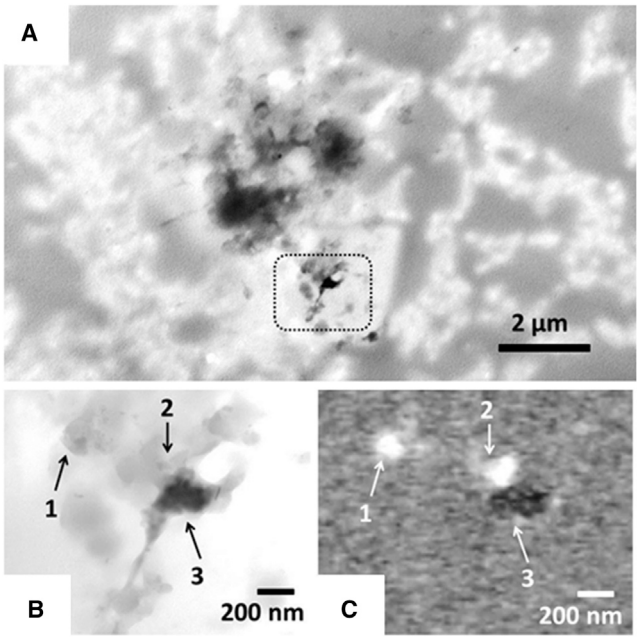

Figure 7. TEM and STXM Comparison of Iron Oxidation State and Structure in Particulate Iron

(A and B) TEM images from an unstained section of cortical tissue from the transgenic mouse tissue sample. The boxed area in (A) is shown at higher magnification in (B).

(C) The corresponding Fe^{2+} and Fe^{3+} distribution map is shown, where bright areas correspond to Fe^{3+}-rich regions and dark areas correspond to Fe^{2+}-rich regions. The labels 1–3 indicate corresponding regions in the TEM image (B) and iron map (C). See also Figure S6.

density and that of iron. This suggests that a seeding mechanism could be involved for these structures, unless the iron can permeate the dense plaques after the protein has been deposited. Consequently, iron may play a much greater role in the development of AD pathology than presently assumed.

Further to this, the observation of substantial levels of ferrous iron (Fe^{2+}) in the aggregates found in this study, is entirely consistent with previous *in vitro* experiments where iron reduction and redox cycling effects were found when $A\beta_{1-42}$ was incubated in the presence of ferric iron (Fe^{3+}) (Everett et al., 2014a, 2014b; Huang et al., 1999; Khan et al., 2006). The formation of redox-active (i.e., ferrous) iron *in vivo* would provide an additional free racial burden via Fenton chemistry. Such ferrous iron would thus contribute further to neurodegeneration via oxidative stress. Ferrous iron was also found in particulate iron deposits of ~50 nm size. Using X-ray absorption and XMCD measurements we were able to show crystalline and ferrimagnetic properties consistent with oxidized and reduced forms of magnetite. Although nanoscale magnetite has been found in AD tissue previously (Collingwood et al., 2008; Kirschvink et al., 1992), these results are the first measurements of the oxidation state of both magnetic and non-magnetic iron in AD tissue *in situ*.

As no attempt was made to prevent postmortem oxidation of tissue in this study, the detection of pure ferrous iron phases suggests other mechanisms must suppress oxidation. One possibility is that the iron is preserved in the ferrous state through binding or coating with amyloid that is in either fibril or amorphous form. The magnetosome membranes in magnetotactic bacteria are an example of just such a mechanism, where they have been found to prevent oxidation of magnetite nanocrystals (Zhu et al., 2015). Here, the protective effect is consistent with the formation of an iron-amyloid complex, as discussed earlier. However, perhaps the most intriguing aspect is the detection of iron with

intermediate oxidation states, providing strong evidence for redox cycling of iron *in vivo*. While it has not yet been proven that the presence of magnetite in the brain is connected to AD pathology, the formation of the highly reduced iron oxides observed here is not expected under normal physiological conditions.

The detection of almost pure Fe^{2+} oxides is consistent with previous nanoelectron diffraction studies on pathological ferritin from AD tissue, where the Fe^{2+} mineral wüstite was found to be the major component of the ferritin core (Quintana et al., 2004). Further to this, earlier work postulated that the malfunction of ferritin could act as a precursor to the formation of ferrous iron-rich minerals (Dobson, 2001). It is possible therefore that ferritin provides the basis for the iron observed here. Such a conclusion is also consistent with our previous *in vitro* experiments where we incubated $A\beta_{1-42}$ with ferrihydrite (the ferric iron oxyhydroxide core found in physiological ferritin) (Everett et al., 2014a). In this previous work we found it was possible to form localized areas containing nanocrystalline magnetite within amyloid aggregates, due to the reductive effect of the iron-amyloid interaction. We also found that the iron was directly correlated with amyloid fibril morphology; a result entirely consistent with the iron-amyloid association in the tissue samples discussed here.

There is some evidence in our study to suggest that the oxidation, crystalline, and magnetic state of the iron associated with plaque material, is linked to the development of the amyloid pathology. For example we found that ferric iron was associated with diffuse plaques which are historically described as early-stage pathological structures (Selkoe, 1994), whereas more particulate and crystalline iron (such as magnetite) was commonly found within dense amorphous regions resembling plaque cores in the transgenic APP/PS1 mouse brain tissue presented here, consistent with prior observations in human Alzheimer's brain tissue (Collingwood et al., 2008; Plascencia-Villa et al., 2016). Given the varying effect of different forms of iron on the relaxation and susceptibility parameters that determine contrast in MRI scans, a link between amyloid morphology and iron could serve as an *in vivo* diagnostic marker to detect the onset and progression of the disease, long before substantial pathology has developed.

Finally, understanding the relationship between iron and the pathology of AD is vital for the development of treatments using metal-modifying drugs such as chelators. To date, such treatments have proved among the most successful in demonstrating benefits in patient trials (Devos et al., 2014). Further to this, a recent study on APP/PS1 transgenic mice similar to those used in the work presented here, revealed that the use of the Fe-chelating drug deferoxamine was able to reduce amyloid plaque formation and prevented iron-induced memory impairments (Guo et al., 2013). Further studies are now required to assess whether iron loading of amyloid structures is unique to transgenic mouse models, or can also be observed in human AD tissue.

SIGNIFICANCE

We have demonstrated that advanced X-ray microscopy techniques can be used to map, with nanoscale resolution and a high degree of chemical specificity, the iron biochemistry associated with amyloid pathology in a transgenic mouse model of Alzheimer's disease. The techniques employed are extremely powerful because of the level of information that can be obtained without processing the brain tissue, which here was unstained and chemically unfixed. We present the first evidence for iron reduced to a pure ferrous state that is directly associated with the dense protein deposits, consistent with amyloid pathology, that form in the cortex of the APP/PS1 mouse but not the wild-type. This is completely consistent with the hypothesis that emerged from prior *in vitro* experiments, and provides new evidence that amyloid-induced chemical reduction of iron could occur *in vivo*. The combined sensitivity and specificity of X-ray microscopy has shown that iron deposits with different morphology and oxidation/magnetic states are not merely localized to the regions of plaque-like deposition in the APP/PS1 mouse as previously suggested, but appear to be an integral part of these structures. Of particular significance, our results indicate that diffuse amyloid deposits (more typical of early-stage amyloid pathology) comprise a bound amyloid-iron composite. The findings are important both for transgenic models and for studies of Alzheimer's disease in humans, to assist with determining the impact of iron chelation on amyloid deposition, and to optimize contrast-agent-free MRI methods to evaluate iron-rich amyloid deposits in the brain. Most importantly, the findings support a model implicating iron in the actual genesis of amyloid deposition in Alzheimer's disease.

STAR★METHODS

Detailed methods are provided in the online version of this paper and include the following:

- KEY RESOURCES TABLE
- CONTACT FOR REAGENT AND RESOURCE SHARING
- EXPERIMENTAL MODEL AND SUBJECT DETAILS
  - Animals
- METHOD DETAILS
  - Preparation of Cortical Tissue Sections
  - Histological Staining
  - Synchrotron X-Ray Spectromicroscopy
  - Transmission Electron Microscopy
- QUANTIFICATION AND STATISTICAL ANALYSIS
- DATA AND SOFTWARE AVAILABILITY

SUPPLEMENTAL INFORMATION

Supplemental Information includes seven figures and can be found with this article online at http://dx.doi.org/10.1016/j.chembiol.2017.07.014.

AUTHOR CONTRIBUTIONS

N.D.T., J.F.C., J.E., J.D., G.v.L., and A.H. designed the experiments and methodologies. J.J.G. performed the animal experiments. N.D.T. and J.E. prepared the STXM and TEM samples. N.D.T., J.E., and J.W. conducted the X-ray synchrotron and TEM experiments. N.D.T. performed the analysis, supervised the project, and wrote the first draft of the manuscript. All authors read and amended the manuscript.

ACKNOWLEDGMENTS

Research described in this paper was performed at the Canadian Light Source, which is funded by the Canada Foundation for Innovation, the Natural Sciences and Engineering Research Council of Canada, the National Research Council Canada, the Canadian Institutes of Health Research, the Government of Saskatchewan, Western Economic Diversification Canada, and the University of Saskatchewan. We are grateful for the assistance of Karen Walker for TEM sample preparation and analysis. J.J.G. was funded by the Health Research Board Ireland and Science Foundation Ireland. J.E. is grateful for doctoral studentship support from Diamond Light Source Ltd and an EPSRC doctoral training grant (EP/P503981). J.F.C. acknowledges partial support for this study from EPSRC grants EP/D066654/1 and EP/K035193/1. N.T. thanks the EPSRC for provision of an Overseas Travel Grant (EP/K00252X/1).

Received: June 19, 2015
Revised: January 19, 2017
Accepted: July 28, 2017
Published: September 7, 2017

SUPPORTING CITATIONS

The following reference appears in the Supplemental Information: Garvie and Buseck, 1998.

REFERENCES

Acosta-Cabronero, J., Williams, G.B., Cardenas-Blanco, A., Arnold, R.J., Lupson, V., and Nestor, P.J. (2013). In vivo quantitative susceptibility mapping (QSM) in Alzheimer's disease. PLoS One *8*, e81093.

Ahmad, S., Kitchin, K.T., and Cullen, W.R. (2000). Arsenic species that cause release of iron from ferritin and generation of activated oxygen. Arch. Biochem. Biophys. *382*, 195–202.

Antharam, V., Collingwood, J.F., Bullivant, J.P., Davidson, M., Chandra, S., Mikhaylova, A., Finnegan, M., Batich, C., and Dobson, J. (2012). Relaxation properties of human hippocampus in Alzheimer's disease using high field MRI microscopy. Neuroimage *59*, 1249–1260.

Coker, V.S., Byrne, J.M., Telling, N.D., Van Der Laan, G., Lloyd, J.R., Hitchcock, A.P., Wang, J., and Pattrick, R.A.D. (2012). Characterisation of the dissimilatory reduction of Fe(III)-oxyhydroxide at the microbe – mineral interface: the application of STXM–XMCD. Geobiology *10*, 347–354.

Collingwood, J.F., Chong, R.K.K., Kasama, T., Cervera-Gontard, L., Dunin-Borkowski, R.E., Perry, G., Pósfai, M., Siedlak, S.L., Simpson, E.T., Smith, M.A., et al. (2008). Three-dimensional tomographic imaging and characterization of iron compounds within Alzheimer's plaque core material. J. Alzheimers Dis. *14*, 235–245.

Collingwood, J.F., Mikhaylova, A., Davidson, M., Batich, C., Streit, W.J., Terry, J., and Dobson, J. (2005). In situ characterization and mapping of iron compounds in Alzheimer's disease tissue. J. Alzheimers Dis. *7*, 267–272.

Collingwood, J.F., and Telling, N.D. (2016). Iron oxides in the human brain. In Iron Oxides: From Nature to Applications, D. Faivre, ed. (Wiley-VCH Verlag), pp. 143–176.

de Groot, F.M.F., de Smit, E., van Schooneveld, M.M., Aramburo, L.R., and Weckhuysen, B.M. (2010). In-situ scanning transmission X-ray microscopy of catalytic solids and related nanomaterials. ChemPhysChem *11*, 951–962.

Devos, D., Moreau, C., Devedjian, J.C., Kluza, J.R., Petrault, M., Laloux, C., Jonneaux, A.L., Ryckewaert, G., and Garçon, G. (2014). Targeting chelatable iron as a therapeutic modality in Parkinson's disease. Antioxid. Redox Signal. *21*, 195–210.

Dickson, T.C., and Vickers, J.C. (2001). The morphological phenotype of beta-amyloid plaques and associated neuritic changes in Alzheimer's disease. Neuroscience *105*, 99–107.

Dobson, J. (2001). Nanoscale biogenic iron oxides in neurodegenerative disease. FEBS Lett. *496*, 1–5.

Dobson, J., and Grassi, P. (1996). Magnetic properties of human hippocampal tissue: evaluation of artefact and contamination sources. Brain Res. Bull. *39*, 255–259.

El Tannir El Tayara, N., Volk, A., Dhenain, M., and Delatour, B. (2007). Transverse relaxation time reflects brain amyloidosis in young APP/PS1 transgenic mice. Magn. Reson. Med. *58*, 179–184.

Everett, J., Céspedes, E., Shelford, L.R., Exley, C., Collingwood, J.F., Dobson, J., van der Laan, G., Jenkins, C.A., Arenholz, E., and Telling, N.D. (2014a). Evidence of redox-active iron formation following aggregation of ferrihydrite and the Alzheimer's disease peptide β-amyloid. Inorg. Chem. *53*, 2803–2809.

Everett, J., Céspedes, E., Shelford, L.R., Exley, C., Collingwood, J.F., Dobson, J., van der Laan, G., Jenkins, C.A., Arenholz, E., and Telling, N.D. (2014b). Ferrous iron formation following the co-aggregation of ferric iron and the Alzheimer's disease peptide β-amyloid (1-42). J. R. Soc. Interface *11*, 20140165.

Fandrich, M., Schmidt, M., and Grigorieff, N. (2011). Recent progress in understanding Alzheimer's beta-amyloid structures. Trends Biochem. Sci. *36*, 338–345.

Gallagher, J.J., Finnegan, M.E., Grehana, B., and Dobson, J. (2012). Modest amyloid deposition is associated with iron dysregulation, microglial activation, and oxidative stress. J. Alzheimers Dis. *28*, 147–161.

Garvie, L.A.J., and Buseck, P.R. (1998). Ratios of ferrous to ferric iron from nanometre-sized areas in minerals. Nature *396*, 667–670.

Guo, C., Wang, T., Zheng, W., Shan, Z.-Y., Teng, W.-P., and Wang, Z.-Y. (2013). Intranasal deferoamine reverses iron-induced memory deficits and inhibits amyloidogenic APP processing in a transgenic mouse model of Alzheimer's disease. Neurobiol. Aging *34*, 562–575.

House, E., Collingwood, J.F., Khan, A., Korchazkina, O., Berthon, G., and Exley, C. (2004). Aluminium, iron, zinc and copper influence the in vitro formation of amyloid fibrils of Aβ42 in a manner which may have consequences for metal chelation therapy in Alzheimer's disease. J. Alzheimers Dis. *6*, 291–301.

Huang, X.D., Atwood, C.S., Hartshorn, M.A., Multhaup, G., Goldstein, L.E., Scarpa, R.C., Cuajungco, M.P., Gray, D.N., Lim, J., Moir, R.D., et al. (1999). The A beta peptide of Alzheimer's disease directly produces hydrogen peroxide through metal ion reduction. Biochemistry *38*, 7609–7616.

Huang, X.D., Atwood, C.S., Moir, R.D., Hartshorn, M.A., Tanzi, R.E., and Bush, A.I. (2004). Trace metal contamination initiates the apparent auto-aggregation, amyloidosis, and oligomerization of Alzheimer's A beta peptides. J. Biol. Inorg. Chem. *9*, 954–960.

Hunter, R.C., Hitchcock, A.P., Dynes, J.J., Obst, M., and Beveridge, T.J. (2008). Mapping the speciation of iron in *Pseudomonas aeruginosa*. Environ. Sci. Technol. *42*, 8766–8772.

Khan, A., Dobson, J.P., and Exley, C. (2006). Redox cycling of iron by A-beta42. Free Radic. Biol. Med. *40*, 557–569.

Kirschvink, J.L., Kobayashi-Kirschvink, A., and Woodford, B.J. (1992). Magnetite biomineralization in the human brain. Proc. Natl. Acad. Sci. USA *89*, 7683–7687.

Leung, B.O., Brash, J.L., and Hitchcock, A.P. (2010). Characterization of biomaterials by soft X-ray spectromicroscopy. Materials *3*, 3911–3938.

Li, J., Hitchcock, A.P., Stöver, H.D.H., and Shirley, I. (2009). A new approach to studying microcapsule wall growth mechanisms. Macromolecules *42*, 2428–2432.

Liu, B., Moloney, A., Meehan, S., Morris, K., Thomas, S.E., Serpell, L.C., Hider, R., Marciniak, S.J., Lomas, D.A., and Crowther, D.C. (2011). Iron promotes the toxicity of amyloid beta peptide by impeding its ordered aggregation. J. Biol. Chem. *286*, 4248–4256.

Mantyh, P.W., Ghilardi, J.R., Rogers, S., Demaster, E., Allen, C.J., Stimson, E.R., and Maggio, J.E. (1993). Aluminum, iron, and zinc ions promote aggregation of physiological concentrations of beta-amyloid peptide. J. Neurochem. *61*, 1171–1174.

Meadowcroft, D.M., Connor, J.R., Smith, M.B., and Yang, Q.X. (2009). Magnetic resonance imaging and histological analysis of beta-amyloid plaques in both human Alzheimer's disease and APP/PS1 transgenic mice. J. Magn. Reson. Imaging *29*, 997–1007.

Meadowcroft, M.D., Peters, D.G., Dewal, R.P., Connor, J.R., and Yang, Q.X. (2014). The effect of iron in MRI and transverse relaxation of amyloid-beta plaques in Alzheimer's disease. NMR Biomed. *28*, 297–305.

Mikula, S., Trotts, I., Stone, J., and Jones, E.G. (2007). Internet-enabled high-resolution brain mapping and virtual microscopy. Neuroimage *35*, 9–15.

Plascencia-Villa, G., Ponce, A., Collingwood, J.F., Arellano-Jimenez, M.J., Zhu, X.W., Rogers, J.T., Betancourt, I., Jose-Yacaman, M., and Perry, G. (2016). High-resolution analytical imaging and electron holography of magnetite particles in amyloid cores of Alzheimer's disease. Sci. Rep. *6*, 24873.

Quintana, C., Cowley, J.M., and Marhicc, C. (2004). Electron nanodiffraction and high-resolution electron microscopy studies of the structure and composition of physiological and pathological ferritin. J. Struct. Biol. *147*, 166–178.

Regan, T.J., Ohldag, H., Stamm, C., Nolting, F., Lüning, J., Stöhr, J., and White, R.L. (2001). Chemical effects at metal/oxide interfaces studied by X-ray-absorption spectroscopy. Phys. Rev. B *64*, 214422.

Rival, T., Page, R.M., Chandraratna, D.S., Sendall, T.J., Ryder, E., Liu, B., Lewis, H., Rosahl, T., Hider, R., Camargo, L.M., et al. (2009). Fenton chemistry and oxidative stress mediate the toxicity of the beta-amyloid peptide in a *Drosophila* model of Alzheimer's disease. Eur. J. Neurosci. *29*, 1335–1347.

Rottkamp, C.A., Raina, A.K., Zhu, X., Gaier, E., Bush, A.I., Atwood, C.S., Chevion, M., Perry, G., and Smith, M.A. (2001). Redox-active iron mediates amyloid-beta toxicity. Free Radic. Biol. Med. *30*, 447–450.

Selkoe, D.J. (1994). Alzheimer's disease: a central role for amyloid. J. Neuropathol. Exp. Neurol. *53*, 438–447.

Shirahama, T., and Cohen, A.S. (1966). A Congo red staining method for epoxy-embedded amyloid. J. Histochem. Cytochem. *14*, 725–729.

Smith, M.A., Harris, P.L., Sayre, L.M., and Perry, G. (1997). Iron accumulation in Alzheimer disease is a source of redox-generated free radicals. Proc. Natl. Acad. Sci. USA *94*, 9866–9868.

Telling, N.D., Coker, V.S., Cutting, R.S., van der Laan, G., Pearce, C.I., Pattrick, R.A.D., Arenholz, E., and Lloyd, J.R. (2009). Remediation of Cr(VI) by biogenic magnetic nanoparticles: an X-ray magnetic circular dichroism study. App Phys. Lett. *95*, 163701–163703.

Tone, B.M., Fakra, S.C., Manganini, S.J., Santelli, C.M., Marcus, M.A., Moffett, J.W., Rouxel, O., German, C.R., and Edwards, K.J. (2009). Preservation of iron(II) by carbon-rich matrices in a hydrothermal plume. Nat. Geosci. *2*, 197–201.

van der Laan, G., and Kirkman, I.W. (1992). The 2p absorption-spectra of 3d transition-metal compounds in tetrahedral and octahedral symmetry. J. Phys. Condens. Matter *4*, 4189–4204.

van der Laan, G. (2013). Applications of soft X-ray magnetic dichroism. J. Phys. Conf. Ser. *430*, 012127.

van der Laan, G., and Figueroa, A.I. (2014). X-ray magnetic circular dichroism - a versatile tool to study magnetism. Coord. Chem. Rev. *277*, 95–129.

Wan, L., Nie, G., Zhang, J., Luo, Y., Zhang, P., Zhang, Z., and Zhao, B. (2011). Beta-amyloid peptide increases levels of iron content and oxidative stress in human cell and *Caenorhabditis elegans* models of Alzheimer disease. Free Radic. Biol. Med. *50*, 122–129.

Wang, D., Li, Y.-Y., Luo, J.-H., and Li, Y.-H. (2014). Age-related iron deposition in the basal ganglia of controls and Alzheimer disease patients quantified using susceptibility weighted imaging. Arch. Gerontol. Geriatr. *59*, 439–449.

Yanker, B.A., and Lu, T. (2009). Amyloid β-protein toxicity and the pathogenesis of Alzheimer disease. J. Biol. Chem. *284*, 4755–4759.

Zhu, X.H., Kalirai, S.S., Hitchcock, A.P., and Bazylinski, D.A. (2015). What is the correct Fe L-23 X-ray absorption spectrum of magnetite? J. Electron Spectrosc. *199*, 19–26.

STAR★METHODS

KEY RESOURCES TABLE

REAGENT or RESOURCE	SOURCE	IDENTIFIER
Chemicals, Peptides, and Recombinant Proteins		
sodium pentobarbital	Merial Animal Health, UK	Euthanol
Sodium cacodylate	Sigma-Aldrich	31533; CAS: 124-65-2 (anhydrous)
Ethanol	Sigma-Aldrich	459836; CAS: 64-17-5
trimethylolpropane triglycidyl ether	Sigma-Aldrich	430269; CAS: 3454-29-3
4,4'-methylenebis-(2-methylcyclohexylamine)	Sigma-Aldrich	369500; CAS: 6864-37-5
Agar	Sigma-Aldrich	A1296; CAS: 9002-18-0
Congo red	Sigma-Aldrich	C6277; CAS: 573-58-0
Deposited Data		
Raw and analyzed data	This paper	http://dx.doi.org/10.21252/keele-0000012
Experimental Models: Organisms/Strains		
SPF C57BL/6 mice	Harlan UK Ltd. (Bicester, UK)	N/A
AβPPswe/PS1dE9 transgenic mice	The Jackson Laboratory (Maine, USA)	N/A
Software and Algorithms		
aXis2000 software package	McMaster University, Canada	http://unicorn.mcmaster.ca/aXis2000.html

CONTACT FOR REAGENT AND RESOURCE SHARING

Further information and requests for resources and reagents should be directed to and will be fulfilled by the Lead Contact, Neil Telling (n.d.telling@keele.ac.uk).

EXPERIMENTAL MODEL AND SUBJECT DETAILS

Animals

Animal maintenance and surgical procedures were performed at Trinity College Institute of Neuroscience, Dublin, Ireland. Specific pathogen-free (SPF) C57BL/6 mice were purchased from Harlan UK Ltd. (Bicester, UK), whilst transgenic animals from an existing colony of AβPPswe/PS1dE9 transgenic mice were purchased from The Jackson Laboratory (Maine, USA), and used to form breeding pairs with the C57BL/6 mice (in an SPF animal housing facility in the Bioresources Unit, Trinity College, Dublin). Mice were maintained according to the regulations and guidelines provided by the local ethical committee. All animals were housed under a 12-h light-dark cycle at an ambient temperature of 22◦C-23°C and were maintained under veterinary supervision throughout. Normal laboratory chow and water were freely available to all animals. Animal experimentation was performed under a license granted by the Minister for Health and Children (Ireland) under the Cruelty to Animals Act 1876 and the European Community Directive, 86/609/EEC, and every effort was made to minimize animal stress.

METHOD DETAILS

Preparation of Cortical Tissue Sections

The mouse cortical brain tissue assessed in this study was obtained from two animals: a female mouse aged 8-9 months that was part of the breeding series from the transgenic AβPPswe/PS1dE9 mice described above and in (Gallagher et al., 2012); and a 14 month old wild-type female mouse. Following anaesthesia, intracardial perfusion was performed for 20 minutes using 0.1M sodium cacodylate (Sigma-Aldrich, UK) to prevent metal leaching effects. To avoid metal contamination the brains were removed using only ceramic tweezers and forceps, and immediately flash frozen using liquid nitrogen before storing at -80°C.

The cortical tissue from the wild-type female mouse was used to develop the methodologies for x-ray spectromicroscopy analysis for this study, and to confirm that the sample preparation procedures (including the use of 0.1M sodium cacodylate, and ethanol dehydration prior to resin embedding) did not lead to unusual iron accumulation or the reduction of ferric iron in the final embedded tissue sections.

The transgenic and wild-type whole brains were transferred in their frozen state to Keele University, where coarse frozen sections were cut inside the cold chamber of a cryotome, using a sapphire knife. The frozen brain hemisphere was cut into four coarse sections approximated by the regions shown on the brain map (Mikula et al., 2007) on the RHS of panel 1 in Figure S7 (see Supplemental

Information). These coarse sections were defrosted in 0.1 M sodium cacodylate and then dehydrated using an ethanol series. Importantly, no chemical fixatives or other reagents were added to the sections. This was to prevent any possible metal leaching or changes in oxidation state of iron within the tissue, although was inevitably to the detriment of the tissue preservation.

Following dehydration the coarse sections were embedded in an aliphatic epoxy resin consisting solely of equimolar amounts of trimethylolpropane triglycidyl ether and 4,4'-methylenebis-(2-methylcyclohexylamine) (Li et al., 2009), and cured for 2 days at 60°C. This resin is suitable for x-ray spectromicroscopy work due to the lack of strong features in its carbon K-absorption edge spectrum (Li et al., 2009). Serial semi-thin sections of 200-300 nm were cut from the embedded blocks using glass blades, and deposited onto either copper TEM grids or silicon nitride membranes. These sections were left unstained for subsequent STXM and TEM investigations. Further thick sections were also cut for parallel histological investigations (see below) but these were not used for the STXM or TEM experiments.

In addition to tissue sections, embedded sections of iron oxide mineral standards were obtained using identical procedures by dispersing the oxides in agar to form gels, and subsequently exposing these gels to 0.1 M sodium cacodylate for 10 mins before dehydrating them using an ethanol series. These samples were then resin embedded and sectioned as described above.

Histological Staining

Following resin embedding of the transgenic mouse brain tissue, thick sections ($\sim$ 1 μm) were cut and mounted on glass slides and stained with toluidine blue dye (LHS, Figure S7). Congo red staining of resin-embedded sections from region 1 was also performed using the protocol by Shirahama (Shirahama and Cohen, 1966). The Congo red stained sections were examined for birefringence under cross-polarized light using an Olympus IX51 microscope. Numerous areas containing structures of $\sim$1 μm size that displayed "apple-green" birefringence characteristic of fibrillar amyloid, were found throughout region 1 (a typical example is shown in Panel 2, Figure S7 in Supplemental Information). The semi-thin sections (200-300nm) cut from region 1 were left unstained and mounted on copper grids and silicon nitride membranes for further study.

Synchrotron X-Ray Spectromicroscopy

X-ray spectromicroscopy experiments were performed with circularly polarised light on the 10ID1 beamline at the Canadian Light Source, using the scanning transmission x-ray microscopy (STXM) endstation. Microscopy images were acquired by tuning the incident beam to a specific x-ray energy, and raster scanning across the area of interest (the x-ray spot size was $\sim$30 nm) with sample exposure times <2 ms per pixel for each image in order to prevent radiation damage.

To obtain maps corresponding to particular elements or oxidation states, paired images were acquired at the desired x-ray absorption feature and at a corresponding energy several eV from the feature, and subtracted from each other. This procedure ensures that only structure containing the spectral feature of interest will appear in the map. For example, an iron map obtained using an image recorded at the 710 eV peak and an off-peak background image at 705 eV, will show only structure containing iron and all other structure will be removed from the image.

Spectromicroscopy was performed by recording a series of images at different x-ray energies across the same area with an exposure time of 2 ms per pixel. The image series was converted to optical density (OD) by recording the incident x-ray flux in a nearby region not containing the sample (for e.g. a hole in the resin). Regions of interest could then be defined within the image series in order to obtain the corresponding spectra.

XMCD measurements were obtained by mounting a silicon nitride membrane containing a tissue section, onto a hollow cylindrical permanent magnet in order to pass the x-ray beam. A reference sample containing synthetic magnetite nanopowder (Sigma-Aldrich, UK) embedded in resin using the identical procedure as for the tissue sample, was mounted on an identical magnet alongside the tissue section. The reference sample was prepared several months after the tissue sections and so no cross sample contamination was possible. As mounted, the magnetic field at the central position of each sample was $\sim$50 mT, which was sufficient to partially magnetise the magnetite nanoparticles. XMCD was obtained by recording an image series across the iron L_3 absorption edge with both left and right circularly polarised x-rays, using an exposure time of 4 ms per pixel.

The two magnets were mounted in an opposing field configuration such that any XMCD signal in the tissue sample should be inverted with respect to the magnetite reference sample, providing additional validation of any apparent XMCD (i.e. magnetic) signal in the tissue. During data analysis the raw data from the magnetite reference sample were subsequently inverted to facilitate comparison with spectra obtained from the tissue sample.

STXM data and image processing were performed using the aXis2000 software package (http://unicorn.mcmaster.ca/aXis2000.html). For iron $L_{2,3}$ x-ray absorption spectra and XMCD, a 3-point smoothing filter was applied to the raw data. The brightness and contrast levels of raw images were adjusted, and composite maps were obtained by converting grey scale images to false colour and then recombining the images as overlays using the ImageJ software package.

Transmission Electron Microscopy

TEM was performed on unstained semi-thin sections using a JEOL 1230 instrument operating at 100 kV. Unless specified otherwise, TEM measurements were conducted on sections after the completion of STXM measurements on the same sections, in order to avoid electron beam damage. However due to the fragility of the sections it was not possible to subject all of them to both STXM and TEM analysis. In the one case where a section previously examined by TEM was subsequently measured by STXM, it was found that the carbon spectrum was substantially altered by electron beam damage and protein maps could no longer be

obtained. However iron mapping, which uses much stronger spectral features and is thus less sensitive to electron beam damage, was still possible on this section.

QUANTIFICATION AND STATISTICAL ANALYSIS

Fits to x-ray absorption data were obtained using a non-linear least squares fitting procedure. Image cross correlation analysis was performed using the ImageJ plugin called ImageCorrelationJ.

DATA AND SOFTWARE AVAILABILITY

Raw and analysed data: http://dx.doi.org/10.21252/keele-0000012